



Inkjet-printed graphene Hall mobility measurements and low-frequency noise characterization

DOI:

[10.1039/C9NR09289G](https://doi.org/10.1039/C9NR09289G)

Document Version

Accepted author manuscript

[Link to publication record in Manchester Research Explorer](#)

Citation for published version (APA):

Calabrese, G., Pimpolari, L., Conti, S., Mavier, F., Majee, S., Worsley, R., Wang, Z., Pieri, F., Basso, G., Pennelli, G., Parvez, K., Brooks, D., Macucci, M., Iannaccone, G., Novoselov, K., Casiraghi, C., & Fiori, G. (2020). Inkjet-printed graphene Hall mobility measurements and low-frequency noise characterization. *Nanoscale*. <https://doi.org/10.1039/C9NR09289G>

Published in:

Nanoscale

Citing this paper

Please note that where the full-text provided on Manchester Research Explorer is the Author Accepted Manuscript or Proof version this may differ from the final Published version. If citing, it is advised that you check and use the publisher's definitive version.

General rights

Copyright and moral rights for the publications made accessible in the Research Explorer are retained by the authors and/or other copyright owners and it is a condition of accessing publications that users recognise and abide by the legal requirements associated with these rights.

Takedown policy

If you believe that this document breaches copyright please refer to the University of Manchester's Takedown Procedures [<http://man.ac.uk/04Y6Bo>] or contact uml.scholarlycommunications@manchester.ac.uk providing relevant details, so we can investigate your claim.



Inkjet-printed graphene Hall mobility measurements and low-frequency noise characterization

Gabriele Calabrese^{1,†}, Lorenzo Pimpolari^{1,†}, Silvia Conti¹, Fabrice Mavier¹, Subimal Majee², Robyn Worsley², Zihao Wang³, Francesco Pieri¹, Giovanni Basso¹, Giovanni Pennelli¹, K. Parvez², D. Brooks², Massimo Macucci¹, Giuseppe Iannaccone¹, Kostya S Novoselov^{3,4,5}, Cinzia Casiraghi², Gianluca Fiori¹

¹Dipartimento di Ingegneria dell'Informazione, Università di Pisa, Pisa 56122, Italy

²Department of Chemistry, University of Manchester, Manchester M13 9PL, UK

³Department of Physics and Astronomy, University of Manchester, Manchester M13 9PL, UK

⁴Chongqing 2D Materials Institute, Liangjiang New Area, Chongqing, 400714, China

⁵Present address: Department of Materials Science and Engineering, National University of Singapore, Singapore 117575, Singapore

[†] These authors contributed equally to this work.

E-mail: gabriele.calabrese@dii.unipi.it

Abstract. We report room temperature Hall mobility measurements, low temperature magnetoresistance analysis and low-frequency noise characterization of inkjet-printed graphene films on fused quartz and SiO₂/Si substrates. We found that thermal annealing in vacuum at 450 °C is a necessary step in order to stabilize the Hall voltage across the devices, allowing their electrical characterization. The printed films present a minimum sheet resistance of 23.3 Ω/sq after annealing, and are *n*-type doped, with carrier concentrations in the low 10²⁰ cm⁻³ range. The charge carrier mobility is found to increase with increasing film thickness, reaching a maximum value of 33 cm² V⁻¹ s⁻¹ for a 480 nm-thick film printed on SiO₂/Si. Low-frequency noise characterization shows a 1/*f* noise behavior and a Hooge parameter in the range of 0.1 – 1. These results represent the first in-depth electrical and noise characterization of transport in inkjet-printed graphene films, able to provide physical insights on the mechanisms at play.

1. Introduction

Since the first observation of exceptional room-temperature mobility [1], graphene has driven intense research efforts, thanks to its superior electrical [2], and thermal [3] properties that, together with chemical and mechanical stability, could lead to its exploitation in flexible and wearable electronics [4, 5]. Graphene was first isolated by mechanical exfoliation of highly oriented pyrolytic graphite [1, 6]. Since then, several techniques have been developed for large scale production, such as Chemical Vapor Deposition (CVD) [7], Si sublimation from SiC [8] and liquid phase exfoliation [9]. Among these techniques, liquid phase exfoliation offers a simple and low-cost approach, compatible with large area deposition methods [10, 11]. Graphene can be synthesized by liquid phase exfoliation using organic solvents [12–14] or stabilizers in water solutions [15–20], and can be thus further exploited in printable electronic applications.

Solution-phase exfoliated graphene inks can be deposited using several techniques, including roll coating [21], spin coating [22], inkjet-printing [10, 23–25], gravure printing [26], flexographic printing [27], and screen printing [28]. Among these techniques, inkjet-printing stands out because it is an additive, non-contact and mask-less approach, with the advantage of a reduced material wastage and a good lateral resolution ($\sim 20\text{-}50\ \mu\text{m}$) [29]. It hence offers a simple, cost-effective and scalable approach for the widespread use of graphene in microelectronic applications.

Inkjet-printed graphene films have been employed for the fabrication of a wide range of electronic and optoelectronic devices and components, such as field effect transistors [10, 30, 31], gas sensors [32], humidity sensors [33], supercapacitors [24, 34–36], solar cell electrodes [37], temperature sensors [38], photodetectors [39], thermoelectrics [40], strain gauges [41], electrochemical biosensors [42], terahertz saturable-absorbers for solid-state lasers [43, 44] and resistor-capacitor low-pass filters [31], to name some examples.

Extensive investigation of the transport properties in mechanically exfoliated [1, 2], CVD-grown [45, 46] and epitaxial graphene [47–49] has been carried out by means of Hall measurements, showing remarkably large carrier mobilities. Only one work reports Hall measurements on solution processed graphene which is subsequently deposited by spray-coating [40], showing reduced room-temperature carrier mobilities of $\sim 20\ \text{cm}^2\ \text{V}^{-1}\ \text{s}^{-1}$. Together with Hall measurements, detailed noise measurements could provide physical insights into the transport mechanisms at play in inkjet-printed graphene films. Low-frequency flicker noise has been extensively investigated in graphene devices fabricated by mechanical exfoliation on SiO_2 [50–55] and hexagonal-boron nitride (h-

BN) [56], and synthesized by CVD on SiO₂ [53, 55], as well as on epitaxial graphene prepared starting from SiC via Si sublimation [57, 58]. Despite the fundamental importance of the results of Hall and noise measurements for device application, an in depth investigation of the electrical and noise properties in inkjet-printed graphene devices has never been performed before.

To this purpose, in this work we report for the first time room temperature Hall measurements, low-temperature magnetoresistance analysis, and low-frequency noise characterization of inkjet-printed graphene films, in order to evaluate their doping and charge carrier density, as well as their low-frequency performance. After thermal annealing, the printed films present a minimum sheet resistance of 23.3 Ω/sq, a room-temperature carrier density in the order of 10²⁰ cm⁻³, a carrier mobility of up to 33 cm² V⁻¹ s⁻¹, and a Hooge parameter in the range of 0.1 – 1.

2. Experimental

2.1. Inkjet-printing and thermal annealing of graphene devices

The graphene ink is prepared by sonication of graphite in water, according to the recipe reported in [18]. The graphene concentration of the ink is 2.5 mg ml⁻¹, as determined by UV-Vis spectroscopy [18]. The physical properties of the ink (viscosity, surface tension, and density) have been optimized in order to enable stable droplet formation and the controlled ejection of individual droplets. In-depth morphological characterization by means of atomic force microscopy and Raman spectroscopy of the graphene flakes composing the ink used in this work was previously reported [18, 41]. The flakes have a lateral size comprised between 50 and 400 nm, with an average value of about 200 nm. They are mainly few-layer thick (< 10 layers) and approximately 20-30% of the flakes are single-layer.

Printing is carried out on fused quartz and SiO₂/Si substrates. Fused quartz substrates are from Heraeus and have a diameter of 30 mm and a thickness of 1 mm. The SiO₂/Si substrates are 4 inch in diameter and consist of 500 micron-thick Si wafers covered by a 300 nm-thick thermal oxide, and are purchased from Graphene Supermarket.

Before printing, Hall bar structures are patterned by standard photolithography of e-beam deposited Cr-Au bilayers (Cr and Au thicknesses are 10 and 100 nm, respectively). After patterning, the substrates are cleaned using acetone and isopropyl alcohol, and dried under N₂ flux. Graphene is printed using a Fujifilm Dimatix DMP-2850 materials deposition system, equipped with a 10 pL nominal volume drop cartridge. Printing is

carried out using one nozzle and keeping the printer plate at a constant temperature of 40 °C. The spacing between individual droplets of the ink is fixed at 40 μm, as optimized in previous works [18, 31].

After printing, the devices are thermally annealed in vacuum at 450 °C for 10 minutes. The thickness (t) of the printed films is determined both before and after annealing through surface profilometry, by using a Bruker Dektak XT system.

2.2. Electrical characterization of printed graphene devices

The sheet resistance of the printed films is measured before (after) annealing in a 4-contact configuration by applying a constant current of 100 μA (1 mA) to the device. The smaller current used before annealing ensures negligible self-heating of the device. Hall effect measurements are performed in vacuum and at room temperature by flowing a current between electrodes labeled as 2 and 5 in Fig. 1 and measuring the Hall voltage (V_H) between electrodes 1 and 3 (4 and 6), using an Agilent 34405A multimeter. For each device, V_H is measured for different values of the applied current in the range of 100 μA to 10 mA. For each value of applied current, V_H is measured both in the absence of a magnetic field and applying a positive and negative field by using a 0.5 T NdFeB permanent magnet external to the vacuum chamber. The magnetic field at the sample location (0.3 T) is measured using a HIRST GM07 Gaussmeter. The density n , and the mobility μ of the charged carriers are calculated from the measured values of V_H as [59]:

$$n = (I \times B) / (q \times t \times V_H), \quad (1)$$

and

$$\mu = 1 / (q \times n \times \rho), \quad (2)$$

where I is the current flowing through the device, B the applied magnetic field, q the elementary charge and ρ the bulk resistivity. n and μ are extracted for each different applied current and their average value is reported in the following.

Magnetoresistance analysis is carried out in a helium-4 cryostat by Cryogenic Limited for a sample fabricated on fused quartz with 80 print passes. The measurements are carried out at 5K using a Stanford SR830 lock-in amplifier. The device longitudinal resistance R_{xx} is symmetrized, while the transverse resistance R_{xy} is antisymmetrized to exclude any influence from R_{xx} .

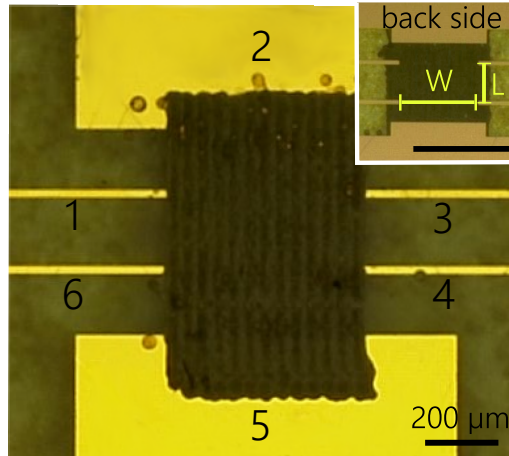


Figure 1. Optical micrograph showing a representative graphene Hall bar fabricated on fused quartz with 40 print passes. In the inset, the backside of the same device is presented. The scale bar in the inset corresponds to 500 μm .

3. Results and discussion

3.1. Hall voltage analysis

Graphene Hall bars are printed on fused quartz and Si/SiO₂ with different number of print passes (20, 40, 60 and 80), in order to investigate the effect of film thickness on both n and μ . For a given substrate, four samples are investigated for each number of print passes. Films prepared with 10 print passes or less are found to be non continuous, and hence are not investigated.

Fig. 1 shows an optical micrograph of a representative Hall bar fabricated on fused quartz with 40 print passes. In the inset, an optical micrograph of the backside of the same device is presented, showing the considered device length (L) and width (W).

Attempts to perform Hall voltage measurements on the as-printed devices result in strong fluctuations of V_H of up to several tens of μV , masking any effects due to the applied magnetic field. In addition, we also observe a continuous drift of V_H in time. This behavior is shown in Fig. 2 (a) for a device fabricated on fused quartz with 20 print passes, for zero, positive, and negative magnetic field and an applied current of 5 mA. We attribute the drift of V_H over time to the observed continuous decrease in sample resistance during measurement. This result is in turn attributed to current-induced self-heating of the device, which likely promotes solvent desorption from the printed films and binder degradation, improving the flake-to-flake electrical conductivity [10, 23].

The observed behavior completely hampers any reproducibility in the measurement of V_H , and prevents the comparison of measurements taken under different magnetic field conditions. It follows that the controlled annealing of inkjet-printed graphene films is an important prerequisite before Hall voltage measurements, in order to obtain devices, whose electrical resistance is not influenced by the flow of current.

Common techniques to desorb the solvents and degrade the binders in printed graphene films consist in post-printing processing methods such as thermal [10, 23, 26, 28, 60, 61], white light [62–64], and laser annealing [65–67]. With the purpose of performing Hall mobility measurements of inkjet-printed graphene, here we employ thermal annealing of the printed films in vacuum.

After annealing in vacuum we observe that for all the investigated devices and different magnetic field conditions, V_H becomes constant over time. This behavior is shown in Fig. 2 (b), for the same device investigated in Fig. 2 (a), but after annealing. Fluctuations and drift in the measured voltage are no longer visible, and we only observe a marginal variation of V_H of $\pm 10 \mu\text{V}$.

In Fig. 2 (b), we observe that V_H measured in the absence of magnetic field (V_{H0}) is at an intermediate value (86.110 mV) as compared to the values measured for positive (86.370 mV) and negative (85.850 mV) applied magnetic field, showing the expected symmetric behavior. The non-zero value for V_{H0} (observed for all the investigated devices), is attributed to asymmetries and inhomogeneities of the printed films. From the sign of V_H , we unambiguously conclude that the dominant charge carriers in our inkjet-printed films are *n*-type, i.e. are electrons.

Together with the observed stabilization of the Hall voltage, annealing in vacuum at 450 °C is found to reduce the average film thickness [see Fig. 2 (c)]. This result is attributed to removal of residual chemicals from the printed films at the employed annealing temperature. Thermal annealing in vacuum at 450 °C is also found to reduce the device resistance by more than one order of magnitude, in agreement with [18]. This result is shown in Fig. 2 (d) for the devices printed on fused quartz. The obtained sheet resistance before annealing is between the 10^2 and $10^3 \Omega/\text{sq}$ range, and decreases to the 10^1 – low $10^2 \Omega/\text{sq}$ range after annealing at 450 °C, as a result of improved flake-to-flake connections due to the removal of residual chemicals. The inkjet-printed films fabricated with 80 print passes on fused quartz (SiO_2), show after thermal annealing an average sheet resistance of 35.5 (35.2) Ω/sq and a minimum sheet resistance of 26.8 (23.3) Ω/sq , which are in line with other results present in the literature [10, 23, 40, 42, 60–62, 65, 67–70].

The average values of n and μ derived from Hall bar analysis for the devices printed

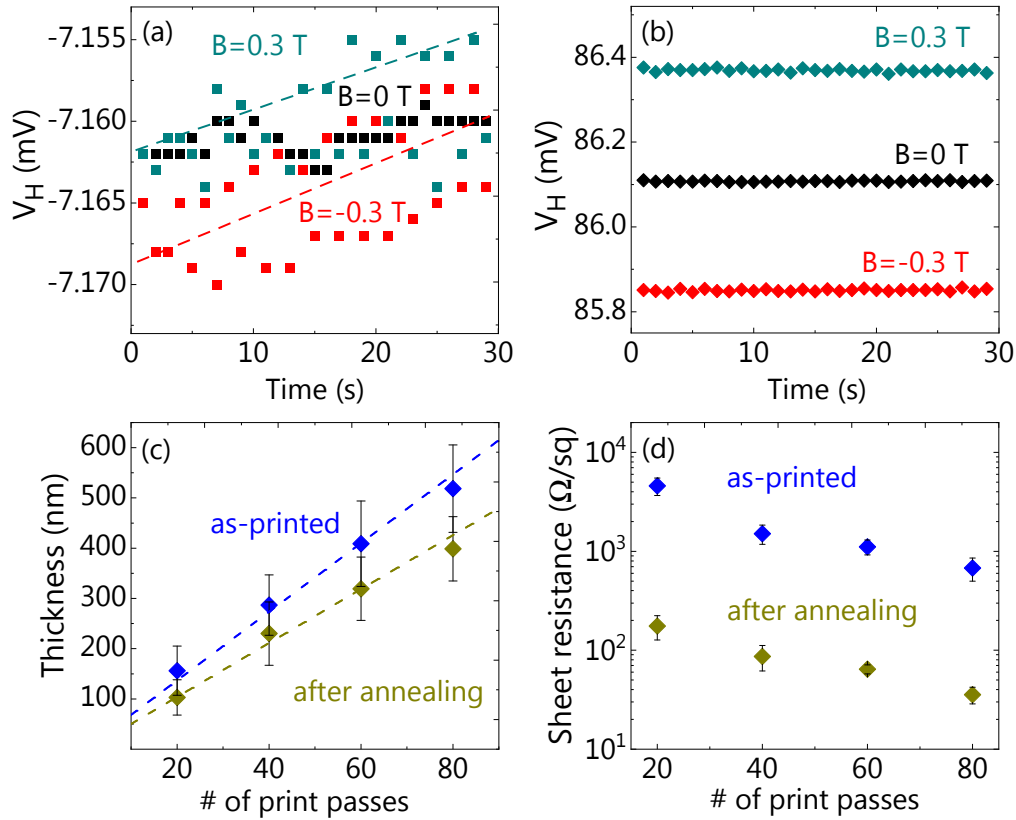


Figure 2. (a) and (b) show V_H as a function of time for positive, negative, and zero applied field, for a sample fabricated with 20 print passes on fused quartz, measured before and after annealing in vacuum, respectively. The dotted lines in (a) are guides to the eye, showing the voltage drift in time. (c) Average film thickness determined by surface profilometry as a function of the number of print passes for the devices fabricated on fused quartz, both before and after thermal annealing in vacuum. The dotted lines show a linear fit of the experimental data. (d) 4-point probe sheet resistance of the printed graphene films on fused quartz as a function of the number of print passes, measured before and after thermal annealing in vacuum. The error bars in (c) and (d) indicate the mean root-mean-square (RMS) roughness and the standard error on the sheet resistance, respectively.

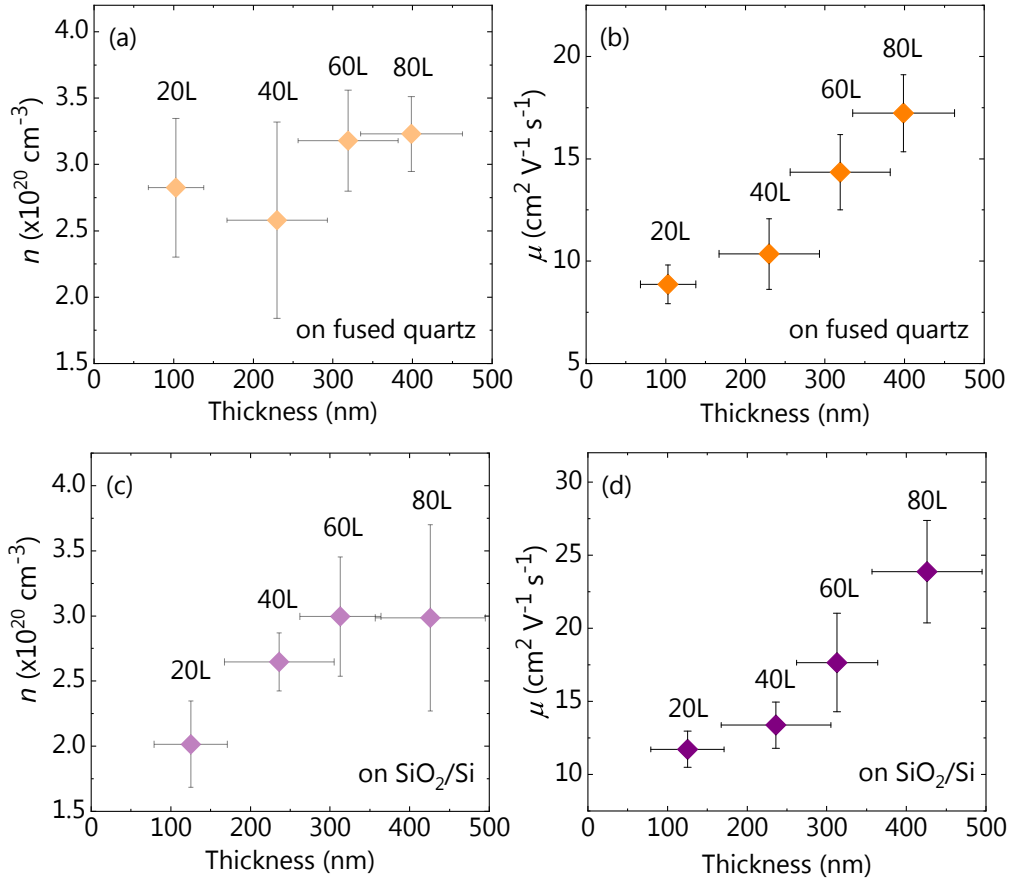


Figure 3. Average values of n and μ determined from Hall bar analysis for the devices printed on fused quartz [(a) and (b)] and on SiO₂ [(c) and (d)], with 20, 40, 60 and 80 print passes. The error bars on the film thickness and on the average values of n and μ represent the mean RMS roughness and the standard error, respectively.

on fused quartz and SiO₂ are reported in Figs. 3 (a) – (d) as a function of film thickness. We observe that the devices printed on the two substrates show the same qualitative behavior. The small differences observed between the results obtained for the samples printed on SiO₂/Si and on fused quartz could be attributed to the different thickness and thermal conductivity of the employed substrates, which is expected to result in different effective substrate temperatures of the printed films upon annealing. The carrier density for all the devices printed on fused quartz and SiO₂ is in the low 10^{20} cm^{-3} range, and remains nearly constant over the investigated range of film thicknesses, no matter the substrate. Such amount of doping (few 10^{12} cm^{-2} per graphene layer) is comparable to

the typical environmental doping observed in graphene samples. However, in the case of solution processed graphene, one has to take into account also the doping due to the solvents and chemical components in the ink. As absorbed moisture is known to result in *p*-type doping, and the doping determined by Hall measurements is *n*-type, this type of doping is expected to arise from chemical residuals in the printed films rather than from the exposure of the samples to air. This speculation is supported by the observation that the results of Hall measurements are the same when the devices are characterized in vacuum or in air. In addition, thermogravimetric analysis carried out for the exploited graphene ink (not reported here) indicates solvent evaporation up to above 500 °C, thus suggesting the existence of residual solvents in the devices investigated in this study (that are annealed at 450 °C). Considering the boiling temperature of each chemical component in the ink [18], we can assume pyrene to be responsible for the observed doping of the printed films. In Figs. 3 (a) and (c) we observe that the thickness of the printed films does not significantly affect *n*. On the other hand, the average value of μ is found to increase with increasing *t* [see Figs. 3 (b) and (d)]. For the samples printed on fused quartz (SiO₂), μ increases from 8.9 (11.7) cm² V⁻¹ s⁻¹ to 17.2 (23.9) cm² V⁻¹ s⁻¹ with increasing average thickness of the printed films from 103 (125) nm to 399 (426) nm. The observed increase of μ with film thickness could be due to several reasons. For example, for larger film thickness the top layers will be further from the substrate therefore less subject to impurity scattering and trapping effects. Another possible explanation is that each printed layer possesses different electrical properties and the probability to achieve paths with low resistance increases as more layers are added to the device. The values of μ determined here for inkjet-printed graphene devices on fused quartz and SiO₂ are in good agreement with the ones reported for spray-coated graphene films [40]. Field effect mobility values ranging from below 1 cm² V⁻¹ s⁻¹ [24, 69] up to 95 cm² V⁻¹ s⁻¹ [10, 69] were previously reported for inkjet-printed graphene films on SiO₂ substrates, while a mobility of 91 cm² V⁻¹ s⁻¹ was reported on textile [30]. However, the values of Hall mobility obtained in this work cannot be directly compared to the previously reported values of field effect mobility.

To gain further insight into the microstructure of our printed films, low temperature magnetoresistance analysis is carried out for one of our printed devices. The magnetoresistance measurement scheme is reported in Fig. 4 (a). The magnetoresistance spectra collected at 5 K for a thermally annealed device in vacuum, fabricated on fused quartz with 80 print passes are reported in Fig. 4 (b). R_{xx} and R_{xy} exhibit the standard low-temperature behavior observed for multilayer graphene films, and R_{xx} shows a distinct

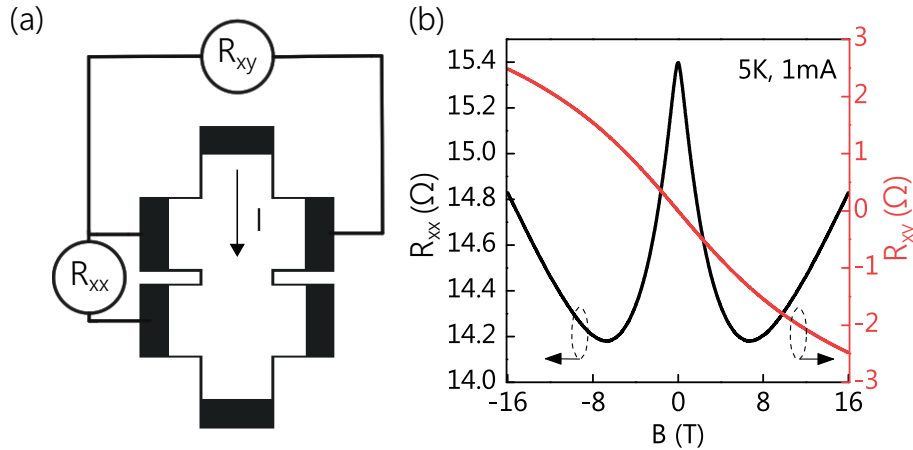


Figure 4. (a) Magnetoresistance measurement scheme and (b) Magnetoresistance spectra taken at 5 K for a device fabricated on fused quartz with 80 print passes, showing the standard weak-localization behavior.

weak-localization peak at $B=0$ T [71]. From the variation of R_{xy} with B we obtain for the investigated device an electron density of $1.5 \times 10^{20} \text{ cm}^{-3}$ and an electron mobility of $69 \text{ cm}^2 \text{ V}^{-1} \text{ s}^{-1}$ at 5 K. This is consistent with a reduced electron-phonon scattering at cryogenic temperatures, as demonstrated for spray-coated graphene [40].

3.2. Low-frequency noise characterization

Low-frequency noise is investigated for samples printed both on fused quartz and on SiO_2 . In particular, we study the noise performance of one device for each kind of substrate and number of print passes, for a total of 8 devices. Low-frequency flicker noise is investigated biasing the device under test (DUT) with a constant current, by using a 12 V lead acid battery in series to a resistor. The value of resistance of the latter, R , is chosen to be much larger than the one of the DUT, in order to approximate a current source (see Fig. 5).

The channel noise voltage (V_x) is amplified using an 80 dB gain, ultralow-noise amplifier (A_1 in Fig. 5), which is described in [72]. The signal is fed to the input of a HP 3562A Digital Signal Analyzer (DSA). The Hall noise voltage is measured between two voltage probes and is amplified using two 60-dB-gain ultra-low noise amplifiers ($EG\&G$ 5004, A_2 and A_3 in Fig. 5, respectively). The signal output of A_2 and A_3 is connected to the input of a differential amplifier (DA), which converts the signal from differential to single ended. The resulting signal is fed to the second input of the DSA. The DSA samples the input noise voltages and computes the voltage noise power spectral densities

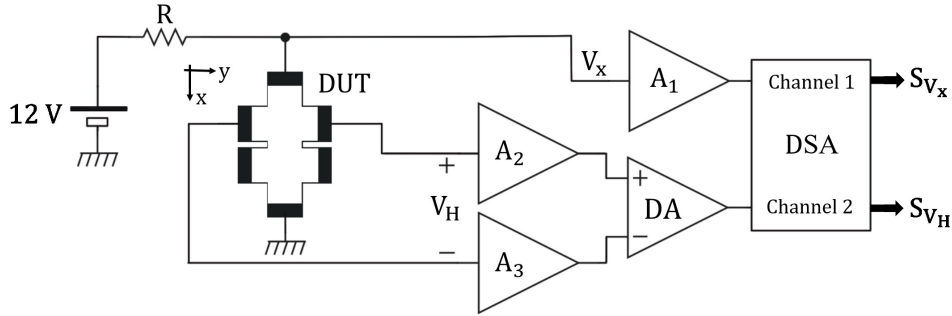


Figure 5. Schematic diagram of the setup used for low-frequency noise characterization. A_1 , A_2 , and A_3 are single-ended amplifiers. DA is a differential amplifier and DSA is a Dynamic Signal Analyzer.

S_{V_x} and S_{V_H} .

Renaming I_x the channel current, its power spectral density (S_{I_x}) can be obtained from the relative voltage power spectral density [73]:

$$S_{I_x} = S_{V_x} / (R \parallel R_{ch})^2, \quad (3)$$

where R_{ch} is the channel noise measured between contacts 2 and 5 in Fig. 1. The S_{I_x} and S_{V_H} spectra as a function of frequency (f), for a device fabricated on a fused quartz substrate with 40 print passes and for different bias currents, are shown in Figs. 6 (a) and (b), respectively.

When the bias current is equal to zero, S_{I_x} and S_{V_H} are equal to the thermal noise of R_{ch} and R_{xy} , respectively. However, for S_{V_H} [Fig. 6 (b)] we also observe a flicker noise component introduced by the amplifiers in the lower frequency range of the recorded spectrum. When a constant current is imposed through the device, flicker noise becomes dominant over the entire frequency range, for both S_{I_x} and S_{V_H} .

The flicker noise power spectral density can be expressed as follows, in accordance to Hooge's law [74]:

$$S_{I_x} = [\alpha_H / (N \times f)] \times I_x^2, \quad (4)$$

where α_H is the Hooge parameter, and N is the total number of carriers in the channel. Noise measurements show the presence of flicker noise at low frequencies, as already reported for exfoliated [50], CVD-grown [55], and epitaxial graphene structures [58]. From Eq. (4) we extract, for our printed devices on fused quartz and SiO_2 , a value of α_H in the range of 0.1 – 1. In particular, for the sample on fused quartz fabricated with 40

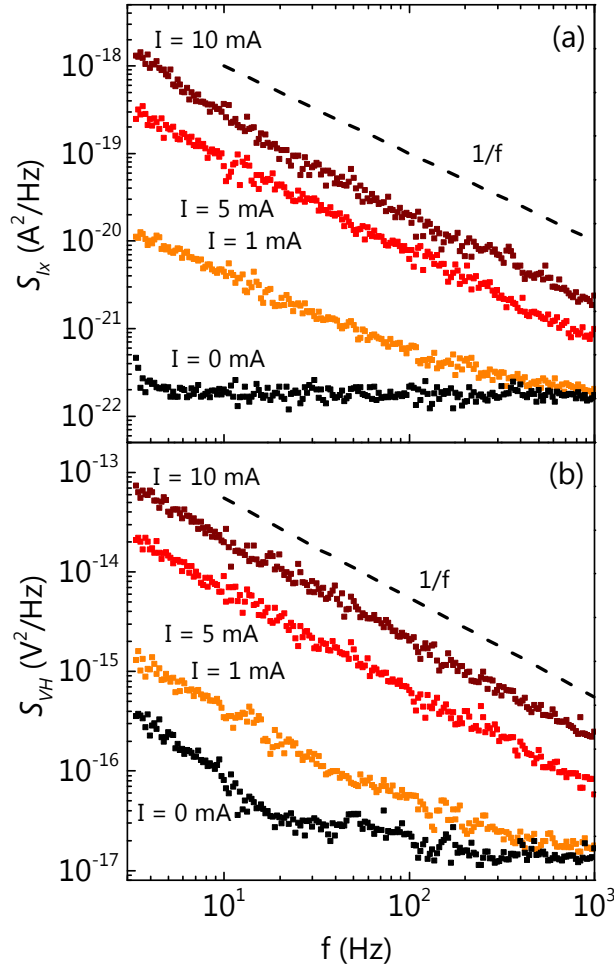


Figure 6. Log-log plot of (a) S_{I_x} and (b) S_{V_H} , as a function of f for a device fabricated on fused quartz with 40 print passes and for different bias currents. As a reference, the $1/f$ slope is shown as a dotted line.

print passes, whose current and voltage noise spectral density spectra are shown in Figs. 6 (a) and (b), we extract $\alpha_H = 0.4$. The obtained values for α_H are larger than those reported for mechanically exfoliated multilayer graphene [51], a result that is attributed to flake-to-flake scattering in inkjet-printed graphene devices. Nevertheless, they are fair when considering the strongly disordered nature of inkjet-printed graphene films. The values of α_H we have obtained are comparable to the values reported for monolayer epitaxial graphene on SiC [75] and hydrazine-reduced graphene oxide [76], while are one order of magnitude larger than those reported for single-layer CVD-grown graphene [55]. The

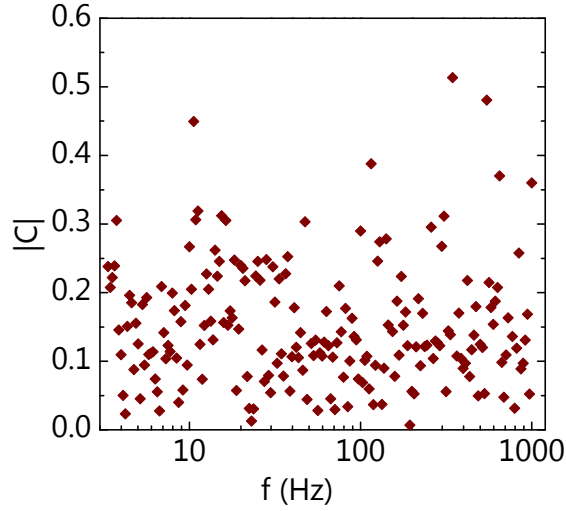


Figure 7. Module of the correlation coefficient as a function of f , for the same device for which the S_{I_x} and S_{V_H} spectra are shown in Figs. 6 (a) and (b), respectively.

obtained values of α_H are also comparable to those extracted from Ref. [77] for liquid-phase exfoliated and drop casted graphene films on Al_2O_3 , assuming a charged carrier mobility of the order of $10 \text{ cm}^2 \text{ V}^{-1} \text{ s}^{-1}$.

Finally, we have calculated the cross spectrum $S_{V_x V_H}$ of the power spectral densities S_{V_x} and S_{V_H} . From this value, we determined the relative correlation coefficient, defined as:

$$C = S_{V_x V_H} / \sqrt{S_{V_x} S_{V_H}}. \quad (5)$$

The module of the correlation coefficient for the device whose noise spectra are shown in Figs. 6 (a) and (b) is presented in Fig. 7 as a function of f . Since $|c| < 0.5$ over the whole range of considered frequencies, the two spectra are not strongly correlated. Therefore we do not expect that a significant improvement of the variance of V_H could be achieved exploiting the information on the time evolution of V_x .

4. Summary

We have reported for the first time Hall mobility measurements, magnetoresistance analysis, and low-frequency noise characterization of inkjet-printed graphene films. Thermal annealing in vacuum at $450 \text{ }^\circ\text{C}$ reduces the sheet resistance of the printed films

by more than one order of magnitude and stabilizes the Hall voltage, thus enabling their electrical characterization. The fabricated devices are found to be *n*-type doped, with electron density in the low 10^{20} cm^{-3} range, a result attributed to doping of inkjet-printed graphene by some of the species composing the ink. The charged carrier mobility monotonically increases with increasing film thickness, reaching a maximum value of $33 \text{ cm}^2 \text{ V}^{-1} \text{ s}^{-1}$ for a 480 nm-thick film. The printed devices show values of α_H ranging from 0.1 to 1, indicating that the noise performance of our inkjet-printed graphene films is comparable to that of monolayer epitaxial graphene and reduced graphene oxide devices. The transport and noise characterization of devices fabricated with the exploited graphene ink indicates it is highly promising for the fabrication of next generation inkjet-printed electronics that benefit from low sheet resistance, good carrier mobility and fair noise performances.

Acknowledgments

This work is financially supported by the ERC grant PEP2D (Contract No. 770047), the H2020 WASP (Contract No. 825213), the Graphene Flagship Core 2 (Contract No. 785219) and by Fondazione Cassa di Risparmio di Lucca. CC, KSN, and KP acknowledge financial support by the Grand Challenge EPSRC grant EP/N010345/1. DB acknowledges funding from the EPSRC in the framework of the CDT Graphene NOWNANO; RW acknowledges the Hewlett- Packard Company for financial support.

References

- [1] Novoselov K S, Geim A K, Morozov S V, Jiang D, Zhang Y, Dubonos S V, Grigorieva I V and Firsov A A 2004 *Science* **306** 666–669
- [2] Stormer H, Kim P, Sikes K, Fudenberg G, Hone J, Bolotin K, Jiang Z and Klima M 2008 *Solid State Communications* **146** 351–355
- [3] Balandin A A, Ghosh S, Bao W, Calizo I, Teweldebrhan D, Miao F and Lau C N 2008 *Nano Letters* **8** 902–907
- [4] Novoselov K S, Fal’ko V, Colombo L, Gellert P, Schwab M, Kim K *et al.* 2012 *Nature* **490** 192
- [5] Ferrari A C, Bonaccorso F, Fal’ko V, Novoselov K S, Roche S, Bøggild P, Borini S, Koppens F H L, Palermo V, Pugno N, Garrido J A, Sordan R, Bianco A, Ballerini L, Prato M, Lidorikis E, Kivioja J, Marinelli C, Ryhänen T, Morpurgo A, Coleman J N,

- Nicolosi V, Colombo L, Fert A, Garcia-Hernandez M, Bachtold A, Schneider G F, Guinea F, Dekker C, Barbone M, Sun Z, Galiotis C, Grigorenko A N, Konstantatos G, Kis A, Katsnelson M, Vandersypen L, Loiseau A, Morandi V, Neumaier D, Treossi E, Pellegrini V, Polini M, Tredicucci A, Williams G M, Hee Hong B, Ahn J H, Min Kim J, Zirath H, van Wees B J, van der Zant H, Occhipinti L, Di Matteo A, Kinloch I A, Seyller T, Quesnel E, Feng X, Teo K, Rupesinghe N, Hakonen P, Neil S R T, Tannock Q, Löfwander T and Kinaret J 2015 *Nanoscale* **7** 4598–4810
- [6] Novoselov K S, Jiang D, Schedin F, Booth T J, Khotkevich V V, Morozov S V and Geim A K 2005 *Proceedings of the National Academy of Sciences* **102** 10451–10453
- [7] Li X, Cai W, An J, Kim S, Nah J, Yang D, Piner R, Velamakanni A, Jung I, Tutuc E *et al.* 2009 *Science* **324** 1312–1314
- [8] De Heer W A, Berger C, Wu X, First P N, Conrad E H, Li X, Li T, Sprinkle M, Hass J, Sadowski M L *et al.* 2007 *Solid State Communications* **143** 92–100
- [9] Hernandez Y, Nicolosi V, Lotya M, Blighe F M, Sun Z, De S, McGovern I T, Holland B, Byrne M, Gun'Ko Y K, Boland J J, Niraj P, Duesberg G, Krishnamurthy S, Goodhue R, Hutchison J, Scardaci V, Ferrari A C and Coleman J N 2008 *Nature Nanotechnology* **3** 563–568
- [10] Torrisi F, Hasan T, Wu W, Sun Z, Lombardo A, Kulmala T S, Hsieh G W, Jung S, Bonaccorso F, Paul P J, Chu D and Ferrari A C 2012 *ACS Nano* **6** 2992–3006
- [11] Torrisi F and Carey T 2018 *Nano Today* **23** 73 – 96
- [12] Hasan T, Torrisi F, Sun Z, Popa D, Nicolosi V, Privitera G, Bonaccorso F and Ferrari A C 2010 *Physica Status Solidi (b)* **247** 2953–2957
- [13] Khan U, Porwal H, O'Neill A, Nawaz K, May P and Coleman J N 2011 *Langmuir* **27** 9077–9082
- [14] Xia Z Y, Pezzini S, Treossi E, Giambastiani G, Corticelli F, Morandi V, Zanelli A, Bellani V and Palermo V 2013 *Advanced Functional Materials* **23** 4684–4693
- [15] Li D, Müller M B, Gilje S, Kaner R B and Wallace G G 2008 *Nature Nanotechnology* **3** 101
- [16] Yang H, Hernandez Y, Schlierf A, Felten A, Eckmann A, Johal S, Louette P, Pireaux J J, Feng X, Mullen K, Palermo V and Casiraghi C 2013 *Carbon* **53** 357 – 365
- [17] Capasso A, Del Rio Castillo A E, Sun H, Ansaldo A, Pellegrini V and Bonaccorso F 2015 *Solid State Communications* **224** 53–63

- [18] McManus D, Vranic S, Withers F, Sanchez-Romaguera V, Macucci M, Yang H, Sorrentino R, Parvez K, Son S k, Iannaccone G, Kostarelos K, Fiori G and Casiraghi C 2017 *Nature Nanotechnology* **12** 343–350
- [19] Karagiannidis P G, Hodge S A, Lombardi L, Tomarchio F, Decorde N, Milana S, Goykhman I, Su Y, Mesite S V, Johnstone D N, Leary R K, Midgley P A, Pugno N M, Torrisi F and Ferrari A C 2017 *ACS Nano* **11** 2742–2755
- [20] Shin Y, Just-Baringo X, Zarattini M, Isherwood L H, Baidak A, Kostarelos K, Larrosa I and Casiraghi C 2019 *Molecular Systems Design & Engineering* **4** 503–510
- [21] Licari J J 2003 *Coating materials for electronic applications: polymers, processing, reliability, testing* (William Andrew)
- [22] Tung V C, Allen M J, Yang Y and Kaner R B 2009 *Nature Nanotechnology* **4** 25
- [23] Secor E B, Prabhmirashi P L, Puntambekar K, Geier M L and Hersam M C 2013 *The Journal of Physical Chemistry Letters* **4** 1347–1351
- [24] Li J, Ye F, Vaziri S, Muhammed M, Lemme M C and Östling M 2013 *Advanced Materials* **25** 3985–3992
- [25] Finn D J, Lotya M, Cunningham G, Smith R J, McCloskey D, Donegan J F and Coleman J N 2014 *Journal of Materials Chemistry C* **2** 925–932
- [26] Secor E B, Lim S, Zhang H, Frisbie C D, Francis L F and Hersam M C 2014 *Advanced Materials* **26** 4533–4538
- [27] Baker J, Deganello D, Gethin D T and Watson T M 2014 *Materials Research Innovations* **18** 86–90
- [28] Hyun W J, Secor E B, Hersam M C, Frisbie C D and Francis L F 2015 *Advanced Materials* **27** 109–115
- [29] Singh M, Haverinen H M, Dhagat P and Jabbour G E 2010 *Advanced Materials* **22** 673–685
- [30] Carey T, Cacovich S, Divitini G, Ren J, Mansouri A, Kim J M, Wang C, Ducati C, Sordan R and Torrisi F 2017 *Nature Communications* **8** 1202
- [31] Worsley R, Pimpolari L, McManus D, Ge N, Ionescu R, Wittkopf J A, Alieva A, Basso G, Macucci M, Iannaccone G, Novoselov K S, Holder H, Fiori G and Casiraghi C 2019 *ACS Nano* **13** 54–60
- [32] Le T, Lakafosis V, Lin Z, Wong C P and Tentzeris M M 2012 Inkjet-printed graphene-based wireless gas sensor modules *Proceedings - Electronic Components and Technology Conference* pp 1003–1008

- [33] Santra S, Hu G, Howe R C T, De Luca A, Ali S Z, Udrea F, Gardner J W, Ray S K, Guha P K and Hasan T 2015 *Scientific Reports* **5** 17374
- [34] Ervin M H, Le L T and Lee W Y 2014 *Electrochimica Acta* **147** 610–616
- [35] El-Kady M F, Shao Y and Kaner R B 2016 *Nature Reviews Materials* **1** 16033
- [36] Sollami Delekta S, Östling M and Li J 2019 *ACS Applied Energy Materials* **2** 158–163
- [37] Dodoo-Arhin D, Howe R C, Hu G, Zhang Y, Hiralal P, Bello A, Amaratunga G and Hasan T 2016 *Carbon* **105** 33 – 41
- [38] Vuorinen T, Niittynen J, Kankkunen T, Kraft T M and Mäntysalo M 2016 *Scientific Reports* **6** 35289
- [39] McManus D, Dal Santo A, Selvasundaram P B, Krupke R, Libassi A and Casiraghi C 2018 *Flexible and Printed Electronics* **3** 034005
- [40] Juntunen T, Jussila H, Ruoho M, Liu S, Hu G, Albrow-Owen T, Ng L W T, Howe R C T, Hasan T, Sun Z and Tittonen I 2018 *Advanced Functional Materials* **28** 1800480
- [41] Casiraghi C, Macucci M, Parvez K, Worsley R, Shin Y, F B, Borri C, Paggi M and Fiori G 2018 *Carbon* **129** 462–467
- [42] Hondred J A, Breger J C, Alves N J, Trammell S A, Walper S A, Medintz I L and Claussen J C 2018 *ACS Applied Materials & Interfaces* **10** 11125–11134
- [43] Bianchi V, Carey T, Viti L, Li L, Linfield E H, Davies A G, Tredicucci A, Yoon D, Karagiannidis P G, Lombardi L *et al.* 2017 *Nature Communications* **8** 15763
- [44] Loiko P, Serres J M, Delekta S S, Kifle E, Bogusławski J, Kowalczyk M, Sotor J, Aguiló M, Díaz F, Griebner U, Petrov V, Popov S, Li J, Mateos X and Östling M 2018 *Optical Materials Express* **8** 2803–2814
- [45] Bae S, Kim H, Lee Y, Xu X, Park J S, Zheng Y, Balakrishnan J, Lei T, Kim H R, Song Y I *et al.* 2010 *Nature Nanotechnology* **5** 574
- [46] Zhou H, Yu W J, Liu L, Cheng R, Chen Y, Huang X, Liu Y, Wang Y, Huang Y and Duan X 2013 *Nature communications* **4** 2096
- [47] Berger C, Song Z, Li T, Li X, Ogbazghi A Y, Feng R, Dai Z, Marchenkov A N, Conrad E H, First P N *et al.* 2004 *The Journal of Physical Chemistry B* **108** 19912–19916
- [48] Berger C, Song Z, Li X, Wu X, Brown N, Naud C, Mayou D, Li T, Hass J, Marchenkov A N *et al.* 2006 *Science* **312** 1191–1196

- [49] Emtsev K V, Bostwick A, Horn K, Jobst J, Kellogg G L, Ley L, McChesney J L, Ohta T, Reshanov S A, Röhrl J *et al.* 2009 *Nature Materials* **8** 203
- [50] Lin Y M and Avouris P 2008 *Nano Letters* **8** 2119–2125
- [51] Pal A N and Ghosh A 2009 *Applied Physics Letters* **95** 082105
- [52] Xu G, Torres C M, Zhang Y, Liu F, Song E B, Wang M, Zhou Y, Zeng C and Wang K L 2010 *Nano Letters* **10** 3312–3317
- [53] Pal A N, Ghatak S, Kochat V, Sneha E, Sampathkumar A, Raghavan S and Ghosh A 2011 *ACS Nano* **5** 2075–2081
- [54] Balandin A A 2013 *Nature Nanotechnology* **8** 549–555
- [55] Arnold H N, Sangwan V K, Schmucker S W, Cress C D, Luck K A, Friedman A L, Robinson J T, Marks T J and Hersam M C 2016 *Applied Physics Letters* **108** 073108
- [56] Kayyalha M and Chen Y P 2015 *Applied Physics Letters* **107** 113101
- [57] Moon J S, Curtis D, Zehnder D, Kim S, Gaskill D K, Jernigan G G, Myers-Ward R L, Eddy C R, Campbell P M, Lee K and Asbeck P 2011 *IEEE Electron Device Letters* **32** 270–272
- [58] Grandchamp B, Fregonese S, Majek C, Hainaut C, Maneux C, Meng N, Happy H and Zimmer T 2012 *IEEE Transactions on Electron Devices* **59** 516–519
- [59] Chien C 2013 *The Hall effect and its applications* (Springer Science & Business Media)
- [60] Wang G, Wang Z, Liu Z, Xue J, Xin G, Yu Q, Lian J and Chen M Y 2015 *Chemical Engineering Journal* **260** 582–589
- [61] He Q, Das S R, Garland N T, Jing D, Hondred J A, Cargill A A, Ding S, Karunakaran C and Claussen J C 2017 *ACS Applied Materials & Interfaces* **9** 12719–12727
- [62] Secor E B, Ahn B Y, Gao T Z, Lewis J A and Hersam M C 2015 *Advanced Materials* **27** 6683–6688
- [63] Arapov K, Bex G, Hendriks R, Rubingh E, Abbel R, de With G and Friedrich H 2016 *Advanced Engineering Materials* **18** 1234–1239
- [64] Secor E B, Gao T Z, Dos Santos M H, Wallace S G, Putz K W and Hersam M C 2017 *ACS Applied Materials & Interfaces* **9** 29418–29423
- [65] Schäfer-Eberwein H, Del S K, Lemme M C, Haring Bolívar P, Li J, Östling M, Kowald T, Bornemann R and Bablich A 2015 *2D Materials* **2** 011003
- [66] Das S R, Nian Q, Cargill A A, Hondred J A, Ding S, Saei M, Cheng G J and Claussen J C 2016 *Nanoscale* **8** 15870–15879

- [67] Das S R, Srinivasan S, Stromberg L R, He Q, Garland N, Straszheim W E, Ajayan P M, Balasubramanian G and Claussen J C 2017 *Nanoscale* **9** 19058–19065
- [68] Majee S, Liu C, Wu B, Zhang S L and Zhang Z B 2017 *Carbon* **114** 77–83
- [69] Yakimchuk E, Soots R, Kotin I and Antonova I 2017 *Current Applied Physics* **17** 1655–1661
- [70] Parvez K, Worsley R, Alieva A, Felten A and Casiraghi C 2019 *Carbon* **149** 213–221
- [71] Morozov S V, Novoselov K S, Katsnelson M, Schedin F, Ponomarenko L, Jiang D and Geim A K 2006 *Physical Review Letters* **97** 016801
- [72] Cannatà G, Scandurra G and Ciofi C 2009 *Review of Scientific Instruments* **80** 114702
- [73] Van der Ziel A 1986 *Noise in solid state devices and circuits* (Wiley-Interscience)
- [74] Hooge F N 1969 *Physics Letters A* **29** 139–140
- [75] Robin A, Lhuillier E, Xu X, Ithurria S, Aubin H, Ouerghi A and Dubertret B 2016 *Scientific Reports* **6** 24909
- [76] Kochat V, Sahoo A, Pal A N, Eashwer S, Ramalingam G, Sampathkumar A, Tero R, Thu T V, Kaushal S, Okada H *et al.* 2015 *IET Circuits, Devices & Systems* **9** 52–58
- [77] Usca G T, Hernandez-Ambato J, Pace C, Caputi L and Tavolaro A 2016 *Applied Surface Science* **380** 268–273